Indentation of plastically graded substrates by sharp indentors

A.E. Giannakopoulos *

Department of Materials Science and Engineering, Massachusetts Institute of Technology, Cambridge, MA 02139, USA

Abstract

The present paper investigates the indentation of plastically graded substrates by sharp indentors. Contact analysis of plastically graded surfaces can be particularly useful in the design of load-bearing devices such as gears, rollers and electric contacts found in many macro- and micro-electro-mechanical systems. Substrates made of plastically graded materials are often encountered in nature or are artificially produced as a result of chemical and/or physical surface treatments. The variation of the plastic properties depends on micro-structural or compositional changes of the material with depth. The analysis of indentation of plastically graded substrates by sharp indentors provide the load-penetration response, as well as the strains and stresses inside the substrate, at maximum loading and at complete unloading. The parametric analysis of the solutions enables the direct correlation of the plastic properties and the load-penetration curves obtained from instrumented indentation tests. The variation of the plastic properties can subsequently be related to important micro-structural parameters such as particle composition, dislocation density and grain size. The results of this work show how surface modifications can induce plastic graded properties that strengthen substrates against contact-induced damage. © 2002 Published by Elsevier Science Ltd.

Keywords: Contact mechanics; Indentation; Plastically graded materials; Surface modifications

1. Introduction

Surface treatments such as case hardening, ion implantation, shot peening, etc., are used to modify mechanical and tribological properties of metals and ceramics without altering their bulk properties. Surface treatments have become routine on commercial scale and are applied to critical components in mechanical, electrical, medical and micro-electro-mechanical devices. The gradual variation of properties at the surface, if chosen properly, can lead to drastic improvements in the performance of the devices by increasing their wear and fatigue resistance due to indentation induced damage. Increasing the hardness of the surface layer, properties such as strength, fatigue, wear, corrosion and oxidation can be significantly improved (Morrison et al., 1990; Fyodorov, 1990; Alfredsson and Olsson, 1999; Stephens et al., 2000). Gradual variations of surface mechanical properties appear naturally (e.g. bones and soils) or are artificial (e.g. functionally gradient materials) and range from macro- to nano-levels of scale. Of particular concern

---

* Address: Department of Civil Engineering, University of Thessaly, Pedion Areos, 383 34 Volos, Greece. Fax: +30-421-074-169.
E-mail address: civileng@civ.uth.gr (A.E. Giannakopoulos).

in the present work is the variation of plastic properties which can be due to temperature gradients, composition gradients, dislocation gradients, surface cold-working, radiation, grain size distribution and fluid or gas content. The scientific and technological significance of surface treatments in creating plastically graded surfaces is underlined in the following examples.

Surface machining and abrasion result to surface layers with yield strength different from that of the substrates. Shot peening, cold rolling, drawing, and forging induce inhomogeneous residual stresses, thus, creating variation of the yield strength with depth. Yield strength variation can result from variation in composition, e.g. particle reinforced components with long range spatial distribution of the reinforcement. Nano-composite technology can localize further this effect. Advances in composite theories permit the prediction of effective plastic behavior, starting from the constituent properties and the composition (Castaneda and Suquet, 1998).

At very small scales, dislocations and grain boundaries can also produce plastically graded substrates. Fourie (1968) showed the existence of a flow stress gradient extending about 2 mm below the surface, along the slip direction of deformed single copper crystals. The lower yield strength of the surface and the variation was related to an increase in the cell size of the dislocation structure near the surface with a decrease in the dislocation density which was observed by electron microscopy. Mughrabi (1971) obtained similar results for single copper crystals that were strained and neutron irradiated. The phenomenon was attributed to the geometric restriction of the surface imposed on the bulk dislocation motion.

Temperature variations due to heat treatment often produce micro-structural changes at the surface. Rapid cooling confines hardening to a relatively narrow region near the surface. Upon annealing, vacancies are depleted near the free surface, creating a layer of lower hardness (Brenner and Kostrov, 1950). Diffusional processes like nitriding, cyaniding, moisture absorption, as well as gradual chemical changes such as oxidation, can change the plastic properties at the surface. In the case-hardening process, the surface hardness increases by diffusing carbon, nitrogen, boron, chromium, aluminum and beryllium atoms from the surrounding medium to the surface. In many alloys, the relation between the yield strength and the amount of the diffused element is known, e.g. carbon or the austenite phase in steel (Tartaglia and Eldis, 1984).

Ion implantation is used extensively to modify the surface mechanical properties in a controlled way (Nastasi et al., 1998). Ion bombardment of the surface creates an inhomogeneous concentration of the implanted species and lattice damage. The yield strength of the defect-rich surface layer follows the variation of the implant concentration, creating a surface gradient in plastic properties (Pethica et al., 1983). For example, implantation of N_2^+ ions into Si and SiC produces a soft amorphous layer (Burnett and Page, 1984). Ion implantation has a small effect on the elastic properties of the substrate. For example, the effect of dissolved hydrogen and oxygen on the elastic moduli of body-centered-cubic (bcc) metals such as V, Nb and Ta is small (Fisher et al., 1975).

Neutron irradiation induces vacancy-inclusion type of defects which tend to pin dislocations and increase the yield strength (Dienes and Vineyard, 1957). For single copper crystal the increase is up to 10-fold, for stainless steel up to 2-fold, for aluminum up to 5-fold and for molybdenum up to 1.5-fold. Irradiation is similar to solid solution hardening, proportional to the 1/2 power of the neutron dose. Neutron irradiation also changes the strain hardening characteristics; irradiated nickel and stainless austenite steels have lower strain hardening than the unirradiated ones. High energy neutron irradiation increases the yield strength but decreases the ductility of 316 and 347 stainless steels. Irradiation increases the yield strength of face-centered-cubic (fcc) metals by a constant amount, increases the yield strength of bcc and hexagonal-closed-packed metals proportionally to the original strength and decreases the yield strength of fcc metals. Neutron irradiation increases the elastic modulus of graphite by a factor of 2, but decreases the modulus of quartz. However, in most polycrystalline materials the elastic modulus change is of the order of 5% and can be neglected.

Other types of radiation, such as deuteron bombardment of SAE1019 steel, harden the surfaces because they produce Frenkel pairs (Meyer, 1954). Electron irradiation on high-purity polycrystalline copper in-

creases modulus by 4% (Simpson and Kerkhoff, 1976). However, electron irradiation on aluminum at liquid nitrogen temperatures decrease the shear modulus by 25% for every 1% of Frenkel pairs created by irradiation (Holder et al., 1974).

An emerging method to investigate plastically graded substrates is the instrumented sharp indentation. The progressive increase or decrease of micro-indentation hardness with decreasing load (which is definitely an indentation size effect) can be related to the presence of a plastically inhomogeneous surface layer (Mott, 1956; Zinkle and Oliver, 1986; Elghazal et al., 2001). However, instrumented indentation tests are often difficult to be interpreted because there is no theory to account for the variation of the yield strength with depth. The present work extends the contact mechanics theory in order to relate the variation of the elastoplastic properties with the load-penetration response, readily obtainable by instrumented sharp indentation.

The paper is arranged as follows. Section 2 contains the analytical results derived for some classes of material models, in particular, the non-linear elastic and the rigid-perfectly plastic. The non-linear elastic model assumes a power law variation of the strain hardening with depth and a square pyramid punch. The rigid-plastic model assumes a linear increasing or decreasing variation of the yield strength with depth and an axisymmetric conical punch. The models used in this work do not always represent actual materials; they are chosen for simplicity and generality of the analysis, and are broad enough to enhance our general understanding of the problem. Section 3 includes the finite element analysis of the material models used in the analysis. The finite element results are compared with the analytical ones and the invert problem is examined: obtain the variation of the elastoplastic properties with depth utilizing the applied force versus penetration depth of an instrumented indentation test. The stress and strain fields at maximum loading and at complete unloading are presented. They provide valuable information for the design of surfaces against contact-induced damage such as wear, fretting fatigue, rolling contact, erosion and low velocity impact. Section 4 gives some comparisons with available experiments from the literature and Section 5 summarizes the conclusions and applications of this work.

2. Analytical results

2.1. Non-linear elastic substrate with power law variation of strain hardening

2.1.1. Basic assumptions

In this model, shown schematically in Fig. 1, the loading parts of the uniaxial stress–strain curves change with depth but do not cross one another. The non-linear elastoplastic deformation response assumes a generalized Ramber–Osgood effective stress–strain constitutive relation which includes both the strain hardening effect and the local variation of the elastoplastic loading response as a function of depth

$$\epsilon_e = (\sigma_e/K)^n (z/d)^k; \quad n \geqslant 1, \ -1 < k < 1. \tag{2.1}$$

In Eq. (2.1), ϵ_e is the von Mises effective total strain, σ_e is the von Mises effective stress, K is a characteristic stress, n is the strain hardening exponent, d is a characteristic length which controls the variation of the elastoplastic properties with depth position $z \geqslant 0$, and k is a non-dimensional parameter which controls the strength of the elastoplastic gradient. If $-1 < k < 0$, the material softens with depth, if $0 < k < 1$, the material hardens with depth. The homogeneous case is obtained for $k = 0$. If $n = 1$, the local response is linear elastic, and if $n \to \infty$, the local response is perfectly plastic. The strain hardening is isotropic and the Poisson ratio, v, is independent of depth.

Suppose that during the loading phase of indentation all material points undergo nearly proportional stressing under the constraint provided by Eq. (2.1). Then, the rate dependent elastoplastic behavior can be
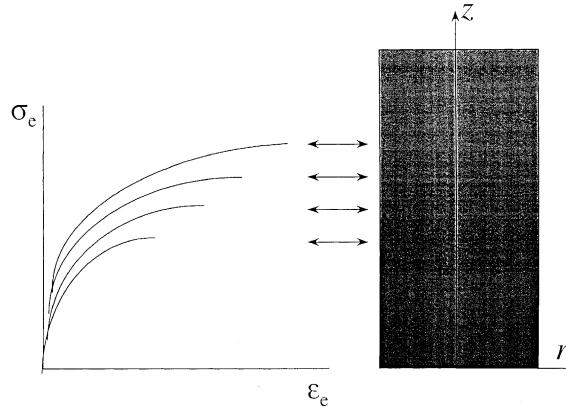
Fig. 1. Uniaxial effective stress–strain curves at different surface depths, under monotonic loading ($\epsilon_e = (\sigma_e/K)^n(z/d)^k$; $n \geqslant 1$, $-1 < k < 1$).

approximated by Henky's total deformation theory. Denote by ϵ_i ($i = 1, 2, 3$) the principal strains and by σ_i ($i = 1, 2, 3$) the corresponding principal stresses. Then, the effective total strain is

$$\epsilon_e = \frac{1}{(1+v)\sqrt{2}} \sqrt{(\epsilon_1 - \epsilon_2)^2 + (\epsilon_2 - \epsilon_3)^2 + (\epsilon_3 - \epsilon_1)^2} \tag{2.2}$$

and the effective stress is

$$\sigma_e = \frac{1}{\sqrt{2}} \sqrt{(\sigma_1 - \sigma_2)^2 + (\sigma_2 - \sigma_3)^2 + (\sigma_3 - \sigma_1)^2}. \tag{2.3}$$

As an example, consider the Ni–Al$_2$O$_3$ composite. Typically, the nickel matrix has elastic modulus 214 GPa, Poisson ratio 0.25, yield strength 178 MPa and strain hardening exponent 5 and the alumina particles have elastic modulus 380 GPa and Poisson ratio 0.25. The plastic properties of the composite depend on the volume composition, c, of the alumina particles. Following the self-consistent method of Castaneda and Suquet (1998), the plastic response of this composite is $\epsilon_e \approx (\sigma_e/735)^5 \exp(-10c)$ in the region $0 \leqslant c \leqslant 0.6$ (σ_e in MPa). Therefore, a graded Ni–Al$_2$O$_3$ composite surface can be described by (2.1) with $K = 735$ MPa and $n = 5$. An approximately logarithmic variation of the alumina composition with depth would produce a power law stress–strain response in accord with Eq. (2.1).

Another example can be obtained from the experimental results of Elghazal et al. (2001) who found that the carbon concentration, c, in AISI 9310 steel affects the uniaxial compression response according to $\epsilon_e \approx (\sigma_e/4.9)^{8.7} (1145 \, c^{0.5})^{-8.7}$ in the region $0.35 \leqslant c \leqslant 0.86$ wt.% (σ_e in MPa). Therefore, a graded carburized steel surface can be described by (2.1) with $K = 4.9$ MPa and $n = 8.7$. An approximately power law variation of the carbon composition with depth would produce a power law stress–strain response in accord with Eq. (2.1).

2.1.2. Point force solution

Fig. 2 shows schematically a point force, P, acting normal to the surface in the z direction and the spherical coordinates (R, η, θ) used in the analysis. A closed form solution of this problem can be obtained, if the Poisson ratio v, the strain hardening exponent n, and the plastic variation exponent k, are related as

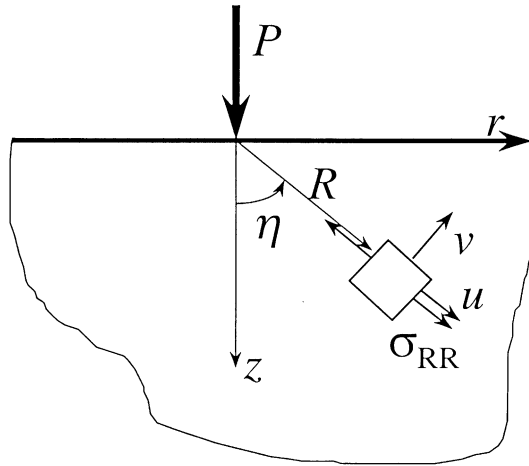$$v = \frac{1}{2n - k}; \quad k < (2n - 2). \tag{2.4}$$

Fig. 2. The point force problem for the non-linear elastic, inhomogeneous material of Fig. 1.

The above choice for the Poisson ratio is not very restrictive and provides substantial simplifications to the analysis. Equilibrium gives the only non-zero stress

$$\sigma_{RR} = -\frac{\Phi(\eta)}{R^2}; \quad \sigma_e = |\sigma_{RR}|, \tag{2.5}$$

where

$$\Phi(\eta) = K[B(\cos\eta)^{(1-k)} d^k]^{1/n}. \tag{2.6}$$

The constant B can be found from global equilibrium

$$P = 2\pi \int_0^{\pi/2} \Phi \cos\eta \sin\eta \, d\eta \tag{2.7}$$

$$\Rightarrow \quad B = \frac{1}{d^k} \left(\frac{P(1+v)}{2\pi vnK} \right)^n. \tag{2.8}$$

The non-zero strains are ϵ_{RR} and $\epsilon_{\eta\eta} = -v\epsilon_{RR}$, where

$$\epsilon_{RR} = -\frac{B\cos\eta}{R^{(2n-k)}}; \quad \epsilon_e = |\epsilon_{RR}|. \tag{2.9}$$

Integrating the strain–displacement relations

$$\epsilon_{RR} = \frac{\partial u}{\partial \eta}, \quad \epsilon_{\eta\eta} = \frac{1}{R}\frac{\partial v}{\partial \eta}, \tag{2.10}$$

we obtain the radial, $u(R, \eta)$, and circumferential, $v(R, \eta)$, displacements

$$u(R, \eta) = \frac{vB\cos\eta}{(1-v)R^{(1/v-1)}}, \tag{2.11}$$

$$v(R, \eta) = -\frac{v^2 B \sin\eta}{(1-v)R^{(1/v-1)}}. \tag{2.12}$$

From Eq. (2.11), it can be shown that the radial surface displacement is zero

$$u(R, \pi/2) = 0. \tag{2.13}$$

The vertical surface displacement is obtained from Eqs. (2.8) and (2.12)

$$v(R, \pi/2) = -\frac{v^2}{(1-v)d^k} \left(\frac{1+v}{2\pi vnK} \right)^n \frac{P^n}{R^{(1/v-1)}}. \tag{2.14}$$

2.1.3. Tetragonal pyramid indentation

The schematic of a tetragonal pyramid indentation is shown in Fig. 3. The included angle of the pyramid is 2γ (for the Vickers indentor, $2\gamma = 136°$). The substrate is initially stress free. The indentor, under normal load P, penetrates the surface to a depth h. In the absence of friction, the contact pressure, $p(x, y)$, can be considered as a distribution of point forces, $p(x, y)\,dx\,dy$. Eq. (2.14) provides the surface vertical displacement due to each point force separately, but it is clear that Eq. (2.14) is non-linear and superposition does not apply in this case. However, if no substantial pile-up occurs at the contact perimeter, which is typically the case for low values of n, then superposition of the point force solution can be used to solve approximately the indentation problem (see Section 3.1 for a finite element verification of the superposition approximation). Following Arutiunian (1959), we retain the principal term of the superposition of the displacements due to the distributed contact pressure, $p(x, y)$. For a tetragonal imprint, with contact surface $4a^2$ ($-a \leqslant x \leqslant a$ and $-a \leqslant y \leqslant a$). Compatibility of the normal displacement between the indentor and the surface gives

$$h - \max(|x|, |y|) \cot \gamma \approx \frac{v^2}{(1-v)d^k} \left(\frac{1+v}{2\pi vnK} \right)^n \left(\int_{-a}^{a} \int_{-a}^{a} \frac{p(x^*, y^*)\,dx^*\,dy^*}{[(x-x^*)^2 + (y-y^*)^2]^{\frac{1-v}{2n\,v}}} \right)^n. \tag{2.15}$$

The contact pressure distribution has 4-fold symmetry, $p(x, y) = p(-x, y) = p(x, -y) = p(-x, -y)$.
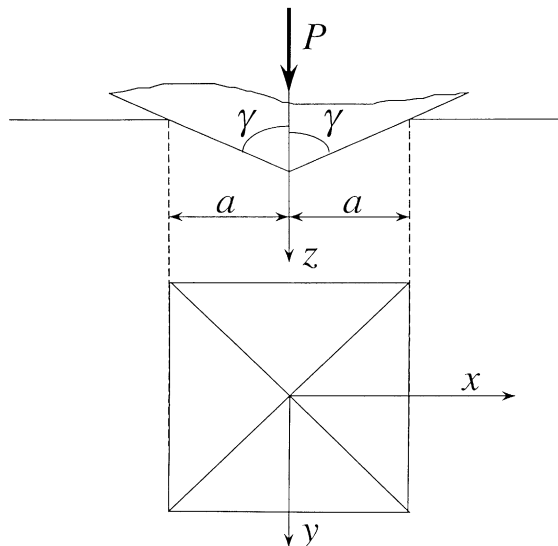

Fig. 3. Schematic of the tetragonal pyramid indentation.

Without loss of generality, the contact pressure distribution can be approximated by the average pressure

$$p(x,y) \approx p_{av} = \frac{P}{4a^2}. \tag{2.16}$$

Then, at the contact center ($x = 0$, $y = 0$, $z = 0$), Eq. (2.15) gives the force–depth (P–h) relation

$$h \approx \left(\frac{P(2n - k + 1)}{8\pi a^2 nK} \right)^n \frac{a^{(1+k)}}{d^k(2n - k)(2n - k - 1)} S^n, \tag{2.17}$$

$$S(m) = 4 \, _2F_1[0.5, m; 1.5; -1]/(1 - m), \tag{2.18}$$

$$m = \frac{2n - k - 1}{2n}; \quad 0 \leqslant m \leqslant 1, \tag{2.19}$$

where $_2F_1[\ ]$ is the generalized hypergeometric function. The above results do not depend critically on the contact pressure distribution. [1]

To estimate the amount of *sinking-in* at the contact perimeter, Eq. (2.15) is solved at ($x = \pm a$, $y = 0$, $z = 0$) or at ($x = 0$, $y = \pm a$, $z = 0$), giving the h–a relation

$$h - a \cot \gamma \approx \left(\frac{P(2n - k + 1)}{8\pi a^2 nK} \right)^n \frac{a^{(1+k)}}{d^k(2n - k)(2n - k - 1)} \bar{S}^n, \tag{2.20}$$

where

$$\bar{S}(m) = 2[(2m - 1)\sqrt{\pi}\Gamma(m - 0.5) - 4m\sqrt{\pi}\Gamma(m + 0.5) - 2(1 - 3m + 2m^2)\Gamma(m - 1)((2m - 1)$$
$$\times \, _2F_1[0.5, m; 1.5; -1] - \, _2F_1[m - 0.5, m; m + 0.5; -1])]/((1 - 2m)^2(m - 1)^2\Gamma(m - 1)), \tag{2.21}$$

where $\Gamma(\ )$ is the gamma function. Combining Eqs. (2.17) and (2.20), we obtain

$$1 - (a/h) \cot \gamma = (\bar{S}/S)^n \approx 1/2^n. \tag{2.22}$$

A closer investigation of (2.22) shows that, for the same indentation depth, sinking-in is increasing with increasing k (surface become stiffer with depth) and is decreasing with increasing n (low strain hardening), however, the influence of the strain hardening exponent n dominates over the stiffness exponent k. Maximum sinking-in occurs for linear response $n = 1$ and minimum sinking-in occurs for $n \gg 1$.

Eqs. (2.17) and (2.22) combined, indicate that

$$h \sim a, \quad P \sim h^{(2n-k)/n}, \quad p_{av} \sim h^{-k/n} \sim P^{-k/(2n-k)}. \tag{2.23}$$

Eq. (2.23) implies an *indentation size effect* due to the inhomogeneous material response ($k \neq 0$). In case of homogeneity ($k = 0$), we recover the classic Kick's law of sharp indentations, $P \sim h^2$, which implies that p_{av} is load independent.

---

[1] Assuming as contact pressure, $p(x,y) = 3P(a - \sqrt{(x^2 + y^2)})/(4a^3)$, as suggested by the finite element analysis of cone indentation, then $S(m) = 8\Gamma(3 - 2m) \, _2F_1[0.5, m - 0.5; 1.5; -1]/\Gamma(4 - 2k) + 8\Gamma(2 - 2m) \, _2F_1[0.5, m; 1.5; -1]/\Gamma(3 - 2k)$, where $\Gamma(\ )$ is the gamma function. The result is numerically similar to Eq. (2.18).

2.2. Rigid-plastic substrate with linear variation of the yield strength

2.2.1. Problem formulation

In the following, the solution of frictionless, axisymmetric indentation of non-homogeneous, rigid-plastic substrate by a rigid cone is presented. The substrate is initially stress free. The deformation is incompressible and axially symmetric, with z being the axis of symmetry and r ($r \geqslant 0$) the radial coordinate. Neglecting the elastic strains in comparison to the plastic strains, the substrate is modeled as rigid-perfectly plastic, with the shear strength to be an explicit function of depth

$$\tau_y = k_c(z) \geqslant 0; \quad z \geqslant 0. \tag{2.24}$$

Tresca yield criterion and associate flow rule are further assumed. The solution invokes the Haar–Karman hypothesis (Hill, 1950) which postulates that the circumferential stress is equal to one of the principal stresses in the meridional plane (r, z), in this case taken to be the maximum tensile stress.

The non-zero stresses are $(\sigma_{rr}, \sigma_{zz}, \sigma_{rz}, \sigma_{\theta\theta})$, however, the Haar–Karman hypothesis requires $\sigma_{\theta\theta}$ to be equal to one of the principal stress in the meridional plane. The reduced problem is hyperbolic with respect to the in-plain stresses $(\sigma_{rr}, \sigma_{zz}, \sigma_{rz})$. Therefore, there exists an orthogonal system of characteristic lines (slip lines), denoted as α and β lines, Fig. 4. The slip lines that pass from a point in the substrate have the property that elements perpendicular to them are under a biaxial compression, $-p$, as well as a critical shear stress, k_c. If ϕ is the inclination of an α-line from the r-axis $(\mathrm{d}z/\mathrm{d}r = \tan\phi)$, then the stress field simplifies as

$$\sigma_{rr} = -p - k_c \sin(2\phi), \quad \sigma_{zz} = -p + k_c \cos(2\phi), \quad \sigma_{rz} = k_c \cos(2\phi), \tag{2.25}$$

$$-p = (\sigma_{rr} + \sigma_{zz})/2, \quad \sigma_{\theta\theta} = -p + k_c. \tag{2.26}$$

In the absence of friction, the surface is free of shear traction, $\sigma_{rz} = 0$, $\phi = \pm\pi/4$ and $p = \pm k_c$.

The equilibrium equations along the α and β lines take the form

$$r(p_{,\alpha} + 2k_c \, \phi_{,\alpha}) + k_c \, (z + r)_{,\alpha} = r \cos\phi \, \mathrm{d}k_c/\mathrm{d}z \quad (\alpha\text{-lines}), \tag{2.27}$$

$$r(p_{,\beta} - 2k_c \, \phi_{,\beta}) - k_c \, (z - r)_{,\beta} = r \sin\phi \, \mathrm{d}k_c/\mathrm{d}z \quad (\beta\text{-lines}), \tag{2.28}$$

where a comma denotes partial differentiation along the α and β lines. The corresponding equations for the plane-strain case were given by Spencer (1961). In the homogeneous case, $\mathrm{d}k_c/\mathrm{d}z = 0$, and Eqs. (2.27) and (2.28) reduce to those of Shield (1955).
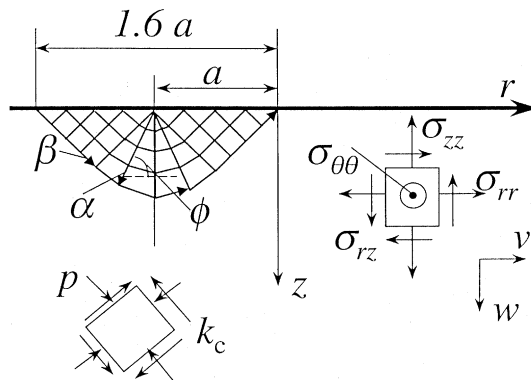

Fig. 4. Schematic of the axisymmetric indentation of a rigid-perfectly plastic substrate.
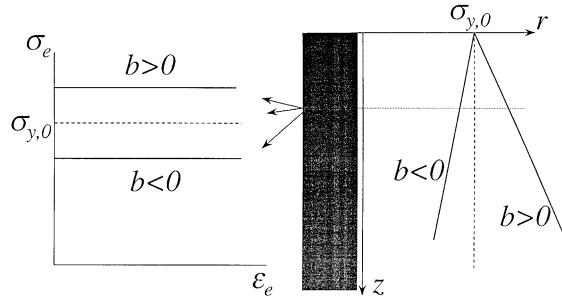
Fig. 5. Yield strength varying linearly with depth for the model of rigid-plastic gradient plasticity ($\sigma_y(z) = \sigma_{y,0} + bz/\sqrt{3}$).

The velocities $\dot{u}$ and $\dot{w}$ in the r and z direction, respectively, change along the characteristic lines as

$$\cos\phi\,\mathrm{d}\dot{u} + \sin\phi\,\mathrm{d}\dot{w} + \dot{u}\,\mathrm{d}s_\alpha/(2r) = 0 \quad (\alpha\text{-lines}), \tag{2.29}$$

$$\sin\phi\,\mathrm{d}\dot{u} - \cos\phi\,\mathrm{d}\dot{w} - \dot{u}\,\mathrm{d}s_\beta/(2r) = 0 \quad (\beta\text{-lines}). \tag{2.30}$$

Eqs. (2.29) and (2.30) satisfy incompressibility and proportionality between the principal stresses and principal strains. At the plastic boundary, $\dot{u} = \dot{w} = 0$, and at the frictionless contact area, $\dot{w} = \text{const.}$ Stability of the deformation can be checked from

$$\sqrt{(\partial\dot{u}/\partial r - \partial\dot{w}/\partial z)^2 + (\partial\dot{u}/\partial z + \partial\dot{w}/\partial r)^2} \geqslant \dot{u}/r \geqslant 0. \tag{2.31}$$

The problem has four basic unknowns $p(r,z)$, $\phi(r,z)$, $\dot{u}(r,z)$ and $\dot{w}(r,z)$. Eqs. (2.27)–(2.30) are the four governing equations which together with the boundary conditions suffice to solve the problem. The velocities along and tangential to the slip lines are assumed continuous, excluding shocks due to velocity discontinuities. To solve the problem, a new method based on a perturbation scheme of the slip lines was used. The solution progresses by simultaneously remapping the slip lines and calculating the pressure, starting from the part of the surface with known tractions. The details of the method are described in Appendix A. On a more physical base, the slip-line solution can be related to dislocation distributions, as shown in Appendix B.

Examples of substrates with constant elastic properties but with yield strength varying with depth are metals with variable grain size, D, solid solution concentration, C, or dislocation spacing, L. Variations of the above parameters with depth result in variations of the yield strength with depth according to the Hall–Petch relation $\sigma_y(z) \sim [D(z)]^{-1/2}$, or the Orowan relations $\sigma_y(z) \sim [C(z)]^{-1/2}$ and $\sigma_y(z) \sim [L(z)]^{-1}$.

2.2.2. Yield strength varying linearly with depth

In case the uniaxial yield strength of the substrate changes linearly with depth, z,

$$\sigma_y(z) = \sigma_{y,0} + bz/\sqrt{3}. \tag{2.32}$$

For $b = 0$, the homogeneous case is recovered, whereas for $b > 0$ the yield strength is increasing with depth and for $b < 0$ the yield strength is decreasing with depth, as shown in Fig. 5. The corresponding variation in shear yield strength is $k_c(z) = \sqrt{3}\sigma_y(z) = k_0 + bz$.

Using the general methodology of the previous section, the average contact pressure for normal contact with a rigid cone of half-apical angle 70° [2] is found to be

$$p_{\mathrm{av}} = 2.75\sigma_{y,0} + 0.853ba, \tag{2.33}$$

---

[2] Such cone geometry represents approximately the geometry of the Vickers and Berkovich pyramid indentors.

where a is the contact radius. Note that for $b = 0$, Eq. (2.33) gives the homogeneous result of Lockett (1963), $p_{av} = 2.75\sigma_{y,0}$. Stability of the indentation loading requires that the contact pressure be compressive inside the contact region. This condition is satisfied, if

$$\sigma_{y,0} + 0.878ba \geqslant 0. \tag{2.34}$$

The constraint (2.34) is always satisfied for $b \geqslant 0$, i.e. for increasing yield strength with depth. The applied load is $P = p_{av}\pi a^2$ and the extend of the rigid-plastic boundary from the center of the contact area at the surface is $1.6a$. The pile-up, z_c, at the contact perimeter can be found from the velocity equations at the contact perimeter, after the pressure is evaluated,

$$\frac{z_c}{a} \approx \frac{0.1032\sigma_{y,0} - 0.1339ba}{1.214\sigma_{y,0} - 1.129ba} \tag{2.35}$$

The depth-contact radius relation is then, $h + z_c = a \cot 70°$. For $b = 0$, the homogeneous result of Lockett (1963), $z_c/a = 0.085$, is recovered. Note that the pile-up does not dependent strongly on the load and is approximately $0.1a$ for most cases.

3. Numerical results

3.1. Power law variation in strain hardening

In this analysis, deformation plasticity was modeled as a non-linear elastic response. The calculations were performed with ABAQUS (1998) commercial finite element code, where the strain hardening variation was included in a special routine at the integration points of the mesh. A mesh with 4625, four-point, axisymmetric elements and 5058 nodes was used, shown in Fig. 6. The mesh and the related far-field boundary conditions were discussed extensively in Giannakopoulos and Suresh (1997), in the analysis of elastic graded materials. The maximum contact radius, a, was resolved by 14 elements in contact with the indentor. Good convergence was achieved when the maximum loading was applied with 30 equal steps. Since the response is non-linear elastic, no unloading was computed in this case. The material was assumed to be locally isotropic, following the Mises flow potential with uniaxial stress–strain law

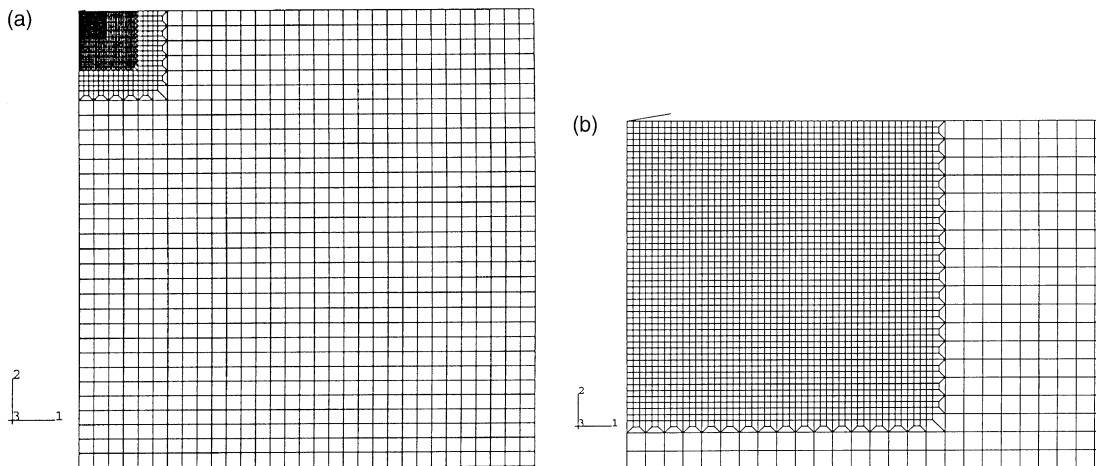$$\epsilon_e = \sigma_e/E + (\sigma_e/K)^n(z/d)^k, \tag{3.1}$$

Fig. 6. (a) The mesh used in the finite element calculations. (b) Detail of the mesh close to the contact region.

which extends Eq. (2.1) to include linear strains. The elastic modulus was chosen to be very high, $E = 10^6$ MPa, to minimize the linear strain components and the other parameters were chosen, $d = 1$ m and $K^n = 10^6$ MPa^n. The strain hardening and the power law exponents varied in the regions $1 \leqslant n \leqslant 3$ and $0 \leqslant k < 1$. The Poisson ratio was constant with depth and depended on n and k according to Eq. (2.4). The indentor was taken to be a rigid cone with angle $2\gamma = 148°$. The analysis assumed frictionless contact and small deformation kinematics.

The contact pressure followed approximately a linear variation in the radial direction

$$p(r) \approx \frac{3P}{\pi a^2}\left(1 - \frac{r}{a}\right). \tag{3.2}$$

The radial displacements at the surface were small, as implied by Eq. (2.13),

$$u(r, z = 0) \approx 10^{-3}h. \tag{3.3}$$

The penetration depth versus contact radius (h–a) relation was

$$1 - (a/h)\cot\gamma \approx 1/\pi^n, \tag{3.4}$$

similar to the prediction of Eq. (2.22). The load–depth (P–h) relation followed

$$h \approx \left(\frac{P(2n - k + 1)}{2\pi a^2 nK}\right)^n \frac{a^{(1+k)}}{d^k(2n - k)(2n - k - 1)}(2 - k)2.5^n, \tag{3.5}$$

in good accord with the prediction of Eq. (2.17). Furthermore, a strong tensile stress was developed close to the contact boundary, in the circumferential direction, $\sigma_{\theta\theta}$, with magnitude depending mainly on the strain hardening exponent n and weakly on k

$$\max \sigma_1 = \sigma_{\theta\theta}(r = a, z = 0) \approx (0.024\text{–}0.24) \times p_{av}. \tag{3.6}$$

It was found that as the strain hardening exponent, n, decreases, the tensile stress increases.

3.2. Linear variation of yield strength with no strain hardening

In this analysis, the elastic modulus and Poisson ratio were kept constant with depth, $E(z) = E = 200$ GPa and $v(z) = v = 0.3$. Incremental plasticity was modeled with Mises yield criterion and associative flow rule. The model assumed a very low, isotropic, linear strain hardening ($d\sigma/d\epsilon = 0.05E$). The yield strength varied linearly with depth, $\sigma_y(z) = 2 \pm 0.9z$ GPa ($0 \leqslant z \leqslant 2$ mm). Under small elastic but large plastic strain kinematics, the z-coordinate refers to the undeformed (Lagrangian) depth coordinate. The indentor was taken to be a rigid cone with angle $2\gamma = 148°$. The analysis assumed frictionless contact. The maximum loading was selected so that the plastic zone be completely inside the zone of variation of the graded plastic properties.

The calculations were performed with ABAQUS (1998) commercial finite element code, where the yield strength variation was included in a special routine at all integration points of the mesh. Large deformation kinematics were included in the analysis. The mesh was similar to the previous case. The maximum contact radius was kept approximately the same in all cases ($a = 0.49$ mm) and was resolved by 12 elements in contact with the indentor. Good convergence was achieved with maximum loading reached in 20 equal steps and complete unloading in 30 equal steps.

The variation of the contact pressure is shown in Fig. 7. The average contact pressure was found to follow the relation
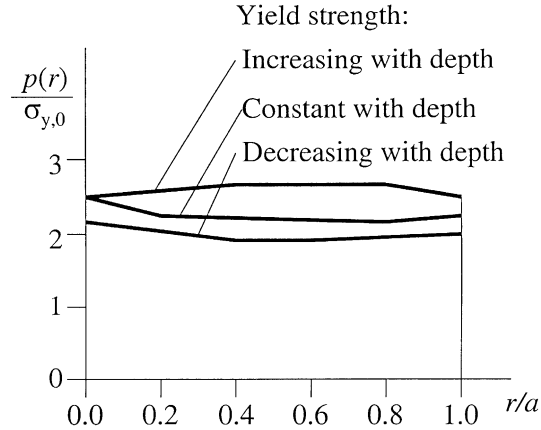
$$p_{av} = 2.2\sigma_{y,0} + 0.8ba. \tag{3.7}$$

Fig. 7. Normalized contact pressures for the homogeneous and graded yield strength ($E = 200$ GPa, $v = 0.3$, $\sigma_y(z) = 2 \pm 0.9z$ GPa and $a = 0.49$ mm).

This result indicates that the elastic strains affect the rigid-plastic prediction of Eq. (2.33). [3] No pile-up or sinking-in at maximum load was found in all the graded cases examined; this result is in accord with Eq. (2.35) which predicts $z_c/a = 0.079$, a value comparable to the finite element resolution of the contact area.

Fig. 8 shows the accumulated effective strain distribution for the cases of constant yield strength (Fig. 8a), increasing yield strength with depth (Fig. 8b) and decreasing yield strength with depth (Fig. 8c). In all cases, the results correspond to the same maximum indentation depth (and the same contact radius). The elastoplastic boundaries are also shown in Fig. 8. The extend of plasticity at the surface is 18% smaller in the case of decreasing yield strength with depth, and about the same for the cases of uniform and of increasing yield strength with depth. The extend of plasticity increases with depth for the case of decreasing yield strength with depth. Comparing with the homogeneous case, the plastic zone is 14% smaller for the case of decreasing yield strength with depth and 10% higher for the case of increasing yield strength with depth, whereas the magnitude of the effective plastic strain is 9% higher for the case of increasing yield strength with depth and 12% lower for the case of decreasing yield strength with depth. Nevertheless, the overall distribution of the effective plastic strain in the substrate is similar in all cases.

The Mises effective stress distribution is shown in Fig. 9 for loading conditions similar to Fig. 8. The elastoplastic boundary is approximately a sphere centered at the contact origin ($r = 0, z = 0$) and of radius $c_p \approx 1.75a$. The Mises stresses, directly below the contact area, follow precisely the variation of the yield strength with depth. Outside the elastoplastic boundary, the Mises stress distribution is independent of the yield strength gradient. This is expected in view of the similar elastic properties assumed in all cases. An important aspect of the solution is the sharp transition of the Mises stress from the outer spherical to the inner layered distribution that occurs close to the elastoplastic boundary.

Upon unloading, the response is elastic for the cases of constant and increasing yield strength with depth. For the case of decreasing yield strength with depth, reverse plasticity may occur at unloading. Numerical simulation showed that yielding upon unloading could occur for decreasing yield strength with depth, provided that

---

[3] Assuming smaller values for σ_y/E, the theoretical solution (2.33) can be approximated closely. For $E = 200$ GPa, $v = 0.3$ and $\sigma_y(z) = 0.2 \pm 0.09z$ GPa, $p_{av} = 2.7\sigma_{y,0} + 0.8ba$.
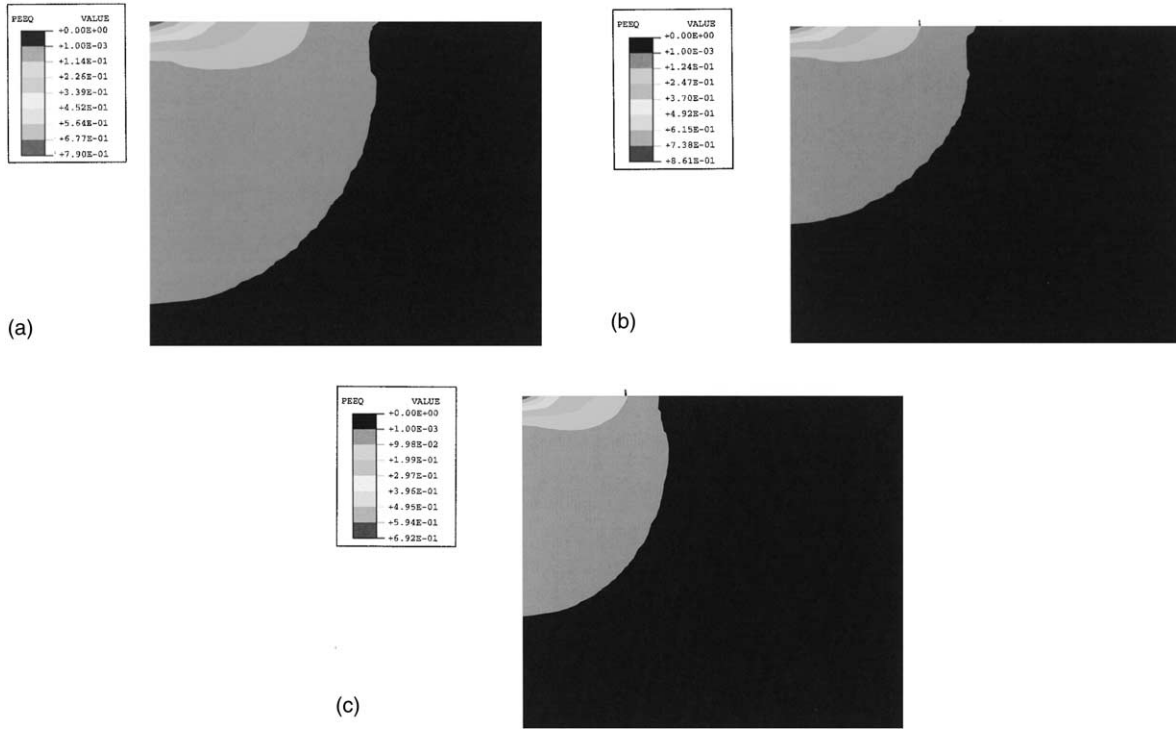
Fig. 8. Distribution of the effective plastic strain at maximum load ($a = 0.49$ mm). Elastic properties: $E = 200$ GPa, $v = 0.3$. Plastic properties: (a) $\sigma_y(z) = 2$ GPa, (b) $\sigma_y(z) = 2 + 0.9z$ GPa, (c) $\sigma_y(z) = 2 - 0.9z$ GPa. All lengths scale with the indicated contact radius.

$$c_p^2 \leqslant 0.2 \frac{E^{1/2}P}{p_{av}^{1/2}\sigma_y(c_p)}, \tag{3.8}$$

where c_p is the elastoplastic boundary developed at maximum loading, P is the maximum load and $\sigma_y(c_p)$ is the yield strength at depth $z = c_p$. The unloading part of the load-penetration curve is approximately the same for all cases where reverse plasticity does not occur.

The development of radial/median cracks and of lateral crack observed in indention of brittle materials is rooted in the circumferential and subsurface tensile residual stresses, respectively (Lawn et al., 1980; Marshall et al., 1982). Therefore, it is of interest to examine the magnitude and position of maximum tensile stresses at maximum loading and at complete unloading.

At maximum loading, the maximum tensile stress appears at the contact boundary and is circumferential, $\sigma_{\theta\theta}$, as expected from the plastic mismatch between the plastic zone and the surrounding material, regardless of the yield strength grading, Fig. 10a. In the case of increasing yield strength with depth, the maximum tensile stress decreases by 3% compared to the constant yield strength case at similar applied loads; however, the location of the maximum tensile stress appears below the surface ($z = c_p, r = 0$), Fig. 10b. The situation is opposite in the case of decreasing yield strength with depth, Fig. 10c; the maximum tensile stress increases by 12% compared to the constant yield strength case at similar applied loads, whereas the location of the maximum tensile stress appears at the surface ($z = 0, r = a_p$) as in the constant yield strength case.

At complete unloading, the maximum tensile stress appears at the contact boundary, as expected from the plastic mismatch between the plastic zone and the surrounding material, regardless of the yield strength grading. In all cases, in addition to the tensile circumferential stresses that appear at the surface
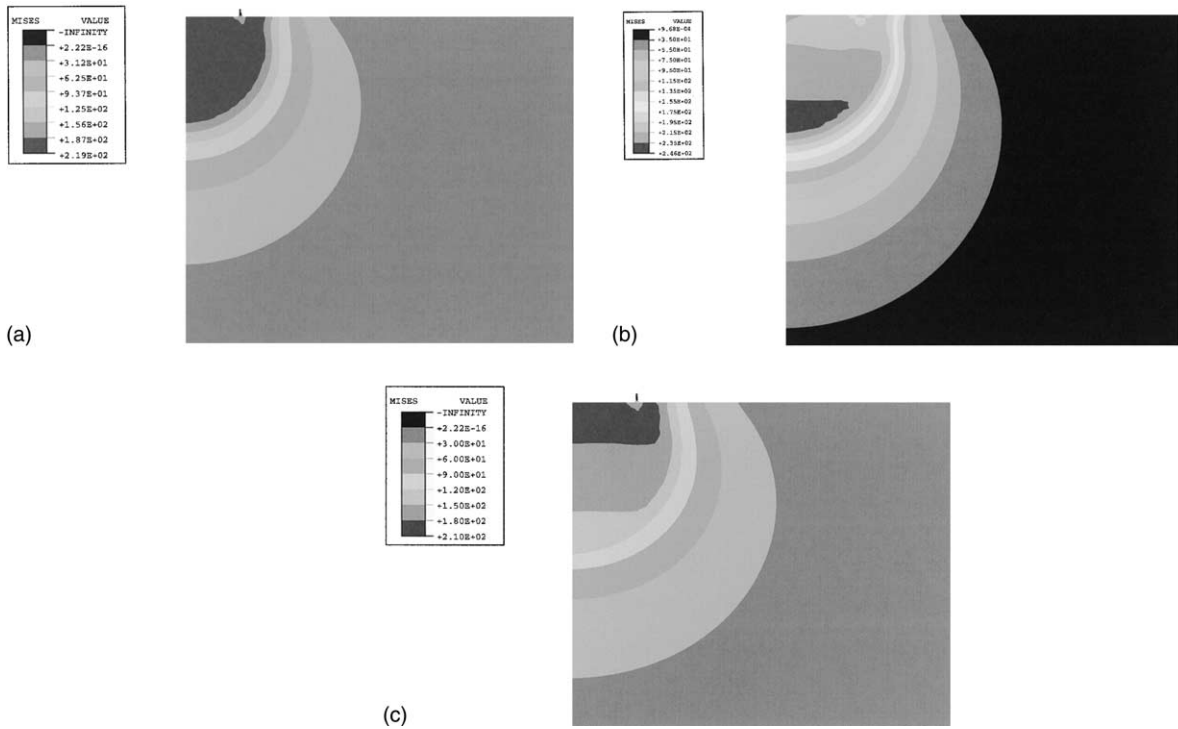
Fig. 9. Distribution of the Mises effective stress at maximum load ($a = 0.49$ mm). Dimensions are in $10^{-1} \times$ MPa. Elastic properties: $E = 200$ GPa, $v = 0.3$. Plastic properties: (a) $\sigma_y(z) = 2$ GPa, (b) $\sigma_y(z) = 2 + 0.9z$ GPa, (c) $\sigma_y(z) = 2 - 0.9z$ GPa. All lengths scale with the indicated contact radius.

($z = 0, r = a_p$), high tensile stresses appear also below the surface ($z = c_p, r = 0$) and are six times lower than the corresponding maximum circumferential stresses, see Figs. 11 and 12. In all cases, the tensile circumferential stresses increase by a factor of about 1.8 from their values at maximum load. In the case of increasing yield strength with depth, the maximum circumferential tensile stress decreases by 8% and the maximum tensile stress below the surface decreases by 13% compared to the constant yield strength case at similar applied loads. The situation is opposite in the case of decreasing yield strength with depth; both the maximum circumferential tensile stress and the maximum tensile stress below the surface increase by 12% compared to the constant yield strength case at similar applied loads. Within less than 4% accuracy, the maximum tensile stress at unloading is

$$\max \sigma_1 = \sigma_{\theta\theta}(r = a, z = 0) \approx \frac{E}{3(1 - v)} \left(\frac{2\sigma_{y,0}}{3p_{av}} \right)^{3/2} \frac{\cot \gamma}{8}. \tag{3.9}$$

It was shown that in sharp indentation of plastically graded substrates, subsequent loading and unloading gave pure elastic response, whereas in layered substrates with interfaces separating materials that have sharply different yield strengths, reverse plastic loading is possible in the vicinity of the interfaces.

4. Comparison with experiments

Instrumented micro- and nano-indentation has been recently used to investigate the composition and hardness profiles of ion-implanted metal surfaces (e.g. Fe, Cr, Ti and steel surfaces), where the composition
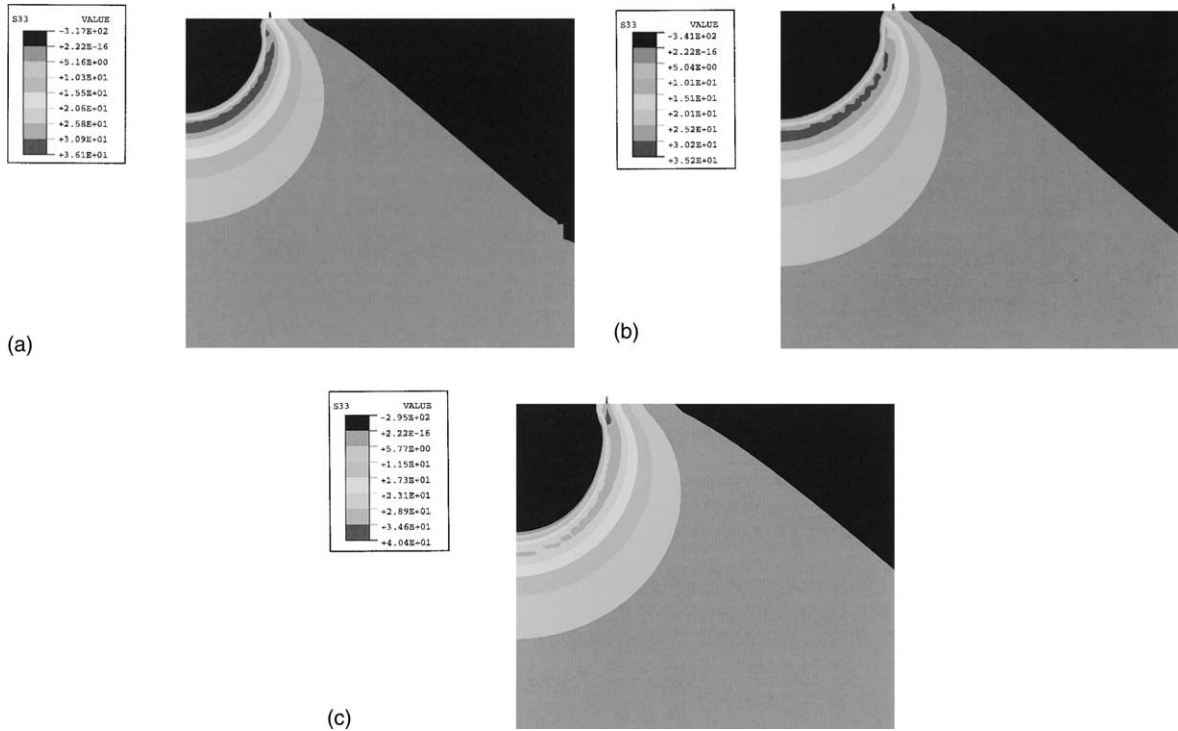
(a)

(b)

(c)

Fig. 10. Distribution of the circumferential tensile stress at maximum load ($a = 0.49$ mm). Dimensions are in $10^{-1} \times$ MPa. Elastic properties: $E = 200$ GPa, $v = 0.3$. Plastic properties: (a) $\sigma_y(z) = 2$ GPa, (b) $\sigma_y(z) = 2 + 0.9z$ GPa, (c) $\sigma_y(z) = 2 - 0.9z$ GPa. All lengths scale with the indicated contact radius.

of ions (e.g. N, Ti, C) was independently evaluated as function of depth. Pethica et al. (1983), for example, found that the ion concentration follows a Gaussian distribution with depth and the local micro-hardness varies proportionally to the ion concentration distribution.

Myers et al. (1998) investigated the nano-indentation response of Ni surface which was ion implanted with 180 keV Ti and 45 keV C. They measured the composition by elastic backscattering of He at 6 MeV, and indented the ion-implanted surface with a Berkovich diamond indentor. In their finite element analysis, Mayer et al. modeled a cone indentation assuming that the yield strength changed stepwise with depth, as shown in Fig. 13. Their final estimates of the yield strengths of the sublayers were found after extensive trial-and-error calculations until the computed P–h curves fitted the experimental one, shown in Fig. 14.

In this work, the experimental P–h curve of Mayer et al. was analyzed assuming that the yield strength decreases linearly with depth within a 200 nm layer, as indicated by the chemical analysis,

$$\sigma_y(z) = 4.7 - 0.0215z; \quad 0 \leqslant z \leqslant 200, \tag{4.1}$$

where σ_y is in GPa and z in nm. Assuming no pile-up or sinking-in, $a \approx h \tan 74°$ and $P = \pi a^2$, and the force–depth relation predicted by Eq. (3.7) is

$$P = (395.1 \, h^2 - 3.970 \, h^3) \times 10^{-6}, \tag{4.2}$$

where P is in mN and h is in nm. Eq. (4.2) is plotted against the experimental result in Fig. 14. The agreement is very good for $0 \leqslant h \leqslant 70$ nm. Note that for $h > 70$ nm the plastic zone extends more than 280 nm and the present analysis breaks down because the yield strength is constant (0.4 GPa) for $z \geqslant 200$ nm.
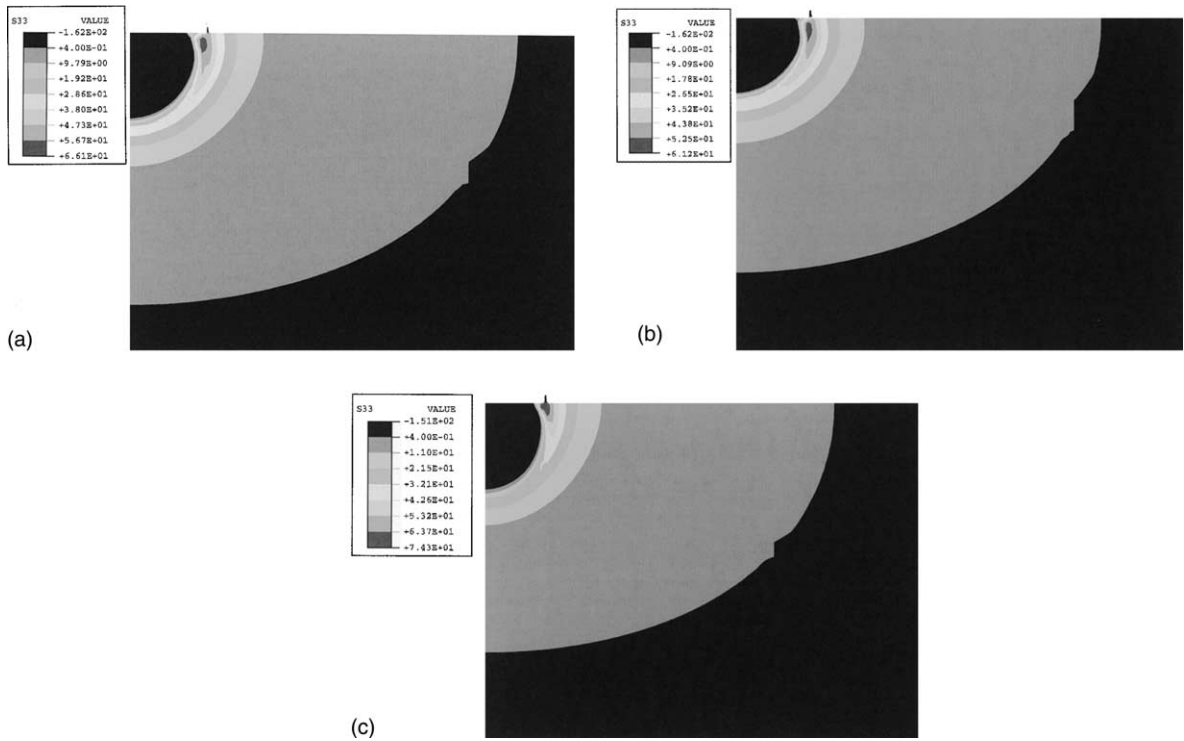
Fig. 11. Distribution of the circumferential tensile stress at complete unloading ($a = 0.49$ mm). Dimensions are in $10^{-1} \times$ MPa. Elastic properties: $E = 200$ GPa, $v = 0.3$. Plastic properties: (a) $\sigma_y(z) = 2$ GPa, (b) $\sigma_y(z) = 2 + 0.9z$ GPa, (c) $\sigma_y(z) = 2 - 0.9z$ GPa. All lengths scale with the indicated contact radius.

5. Conclusions

This work examined the normal indentation of plastically graded substrates by sharp indentors. In the analysis, local, non-linear elasticity and slip-line plasticity theories were used, modeling the graded plastic properties explicitly as functions of depth from the surface. For linear variations of the yield strength and for power law variation of the strain hardening with depth, the load-penetration responses were derived in closed forms. The average contact pressure indicates an explicit indentation size effect, i.e. dependency of the hardness with indentation load. Finite elements capable of modeling any mechanical property variation with depth were developed. Available experimental work was analyzed with the present theory. The derived closed form solutions enable the formulation of the inverse problem of estimating the variation of the plastic properties with depth by fitting the analytical predictions to the load-penetration curves obtained from instrumented sharp indentation tests. The variation of the plastic properties can be correlated to composition or dislocation variation with depth.

In addition, strain and stress distributions inside the substrate at maximum loading and at complete unloading were obtained. The Mises effective stress varied in accord with the gradation of the yield strength, whereas the effective plastic strain distribution did not change much. Upon complete unloading, it was found that surfaces with increasing yield strength with depth suppress the residual tensile stresses, whereas surfaces with decreasing yield strength with depth enhance them. It is clear that surface modifications that result in substrates with increasing yield strength with depth are desirable. Such substrates can suppress effectively the residual tensile stresses that induce radial and lateral cracking, delamination and
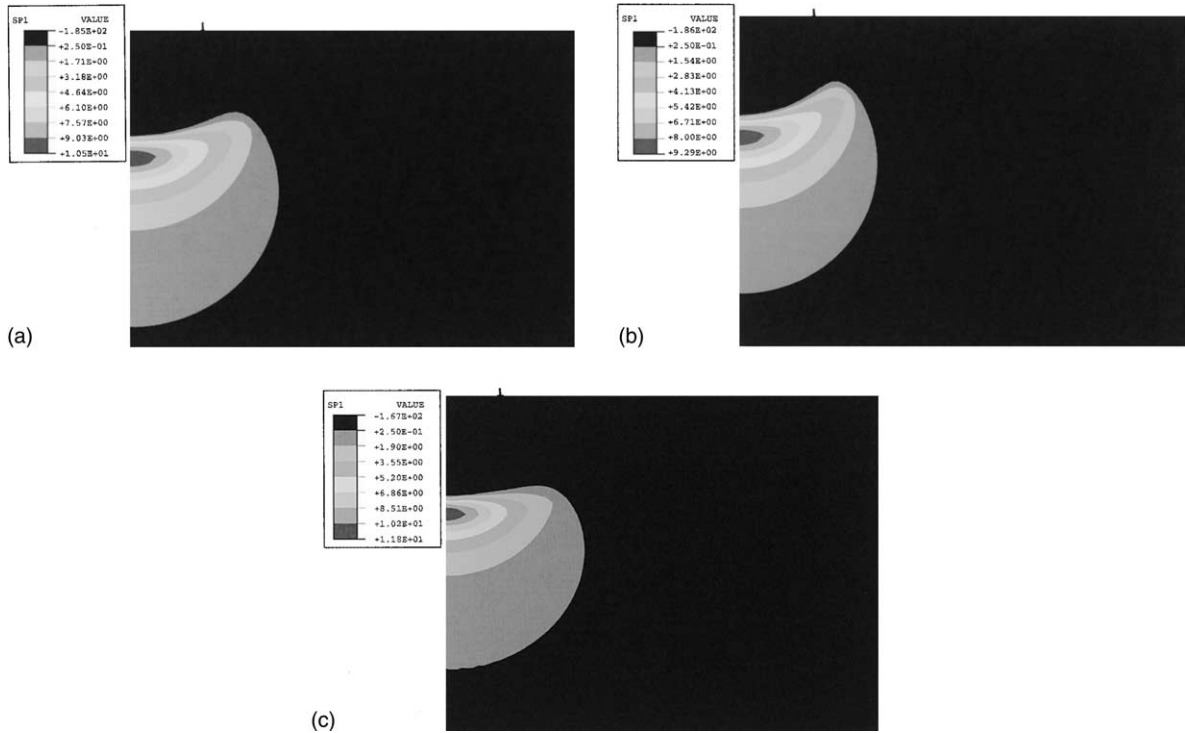
Fig. 12. Distribution of the maximum tensile stress below the surface at complete unloading ($a = 0.49$ mm). Dimensions are in $10^{-1} \times$ MPa. Elastic properties: $E = 200$ GPa, $v = 0.3$. Plastic properties: (a) $\sigma_y(z) = 2$ GPa, (b) $\sigma_y(z) = 2 + 0.9z$ GPa, (c) $\sigma_y(z) = 2 - 0.9z$ GPa. All lengths scale with the indicated contact radius.
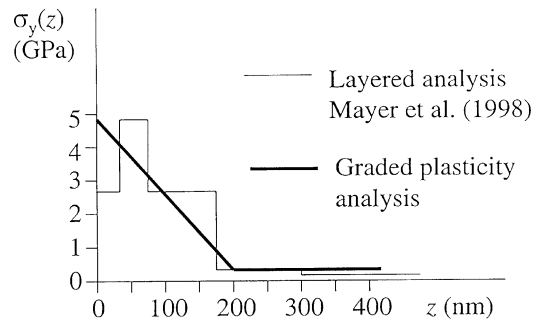

Fig. 13. Yield strength as a function of depth for unimplanted Ni and for Ni implanted with 180 keV Ti and 45 keV C, as extracted from simulation fits to indentation data (Myers et al., 1998). The continuum line is according to the present model of plastic gradient theory.

excessive plastic deformation. The results also suggest that radial cracking at loading can be most effectively suppressed by tailoring substrates with low strain hardening exponent at the surface.

The practical applications of the present analysis are numerous and suggest the use of instrumented sharp indentation for
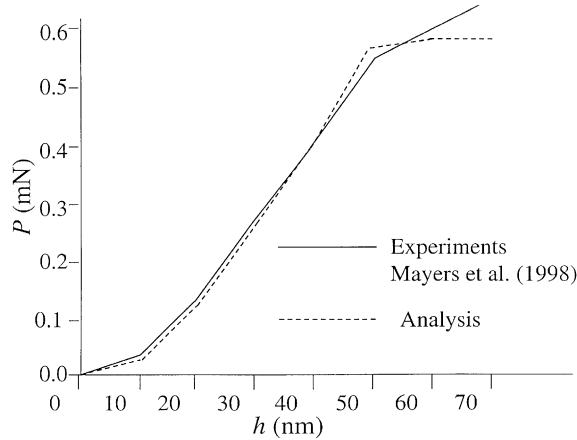
Fig. 14. Indentation data and fitted finite element simulation for Ni implanted with 180 keV Ti and 45 keV C (Myers et al., 1998). The result from the present plastic gradient theory is also given for comparison.

(a) quality control of surface treatments such as ion implantation, case hardening and irradiation, as well as surface modifications due to unwanted environmental effects such as oxidation, radiation and corrosion,
(b) inspection procedures in aerospace, civil, naval, elecromechanical and nuclear components such as gears, load-bearing spheres and cylinders, armory plates, radiation-protection plates, nuclear material containers, electric and magnetic contacts,
(c) optimization of surface treatments that strengthen the substrates against delamination and spalling, rolling contact, wear and fretting fatigue related failures.

Acknowledgements

Appendix A. A perturbation method for slip-line analysis

Following Richmond and Morrison (1968), (p, ϕ, r, z) are expanded it terms of power series of a small quantity ϵ

$$p(\alpha, \beta) = p^0(\alpha, \beta) + \epsilon p^*(\alpha, \beta) + \epsilon^2 p^{**}(\alpha, \beta) + \cdots, \tag{A.1}$$

$$\phi(\alpha, \beta) = \phi^0(\alpha, \beta) + \epsilon \phi^*(\alpha, \beta) + \epsilon^2 \phi^{**}(\alpha, \beta) + \cdots, \tag{A.2}$$

$$r(\alpha, \beta) = r^0(\alpha, \beta) + \epsilon r^*(\alpha, \beta) + \epsilon^2 r^{**}(\alpha, \beta) + \cdots, \tag{A.3}$$

$$z(\alpha, \beta) = z^0(\alpha, \beta) + \epsilon z^*(\alpha, \beta) + \epsilon^2 z^{**}(\alpha, \beta) + \cdots, \tag{A.4}$$

and the trigonometric quantities

$$\cos \phi = \cos \phi^0 - \sin \phi^0 \ [\epsilon \phi^*(\alpha, \beta) + \epsilon^2 \phi^{**}(\alpha, \beta) + \cdots], \tag{A.5}$$

$$\sin \phi = \sin \phi^0 + \cos \phi^0 \ [\epsilon \phi^*(\alpha, \beta) + \epsilon^2 \phi^{**}(\alpha, \beta) + \cdots]. \tag{A.6}$$

The above expansions are inserted in the equations of equilibrium (2.27) and (2.28) and in the equations of the characteristic lines

$$\cos \phi \, z_{,\alpha} = \sin \phi \, r_{,\alpha} \ \ (\alpha\text{-lines}), \tag{A.7}$$

$$\sin \phi \, z_{,\beta} = -\cos \phi \ r_{,\beta} \ \ (\beta\text{-lines}). \tag{A.8}$$

From the transformed Eqs. (2.27), (2.28), (A.7) and (A.8), the terms of like order powers of ϵ are then grouped and equated to zero.

The initial net of the characteristic lines is given by the analogous plane-strain problem which defines r^0 and z^0. Then, p^0 and ϕ^0 can be found by integrating the equilibrium equations of zeroth order in ϵ. The solution proceeds by solving sequentially simple systems of four, first order, partial differential equations which result from collecting like order power terms of ϵ. The integration starts from outside the contact surface where $p = \pm k_c(0)$ and $\phi = \pm \pi/4$. For the case of $k_c(z) = k_0 + bz$, the starting part of the surface was divided into 14 equal increments and the sheared area was covered with 14-$\alpha \times$ 14-β slip lines, with $\epsilon = b/k_0$. The solution converges, if b/k_0 is smaller than the contact radius.

Appendix B. Slip-line analysis and continuous distribution of dislocations

In the mathematical theory of plasticity, the slip lines can be related to the trajectories of the dislocation motion (Mura, 1965). The distribution of dislocations is assumed continuous and the dislocation density tensor, a_{ij}, is related to the total Burger's vector per unit area. In the case of axisymmetric rigid-perfectly plastic indentation, the analysis is simplified by assuming that all dislocations are circular loops of edge type, concentric to the axis of symmetry. For such cases, the dislocation density tensor has two non-zero components, $a_{3\alpha}$ and $a_{3\beta}$, corresponding to the orthogonal coordinates created by the slip lines (Kroner, 1958). The measure of the change of the orientation of the slip-line directions is given by the curvature tensor which has components $\partial \phi / \partial s_\alpha$ and $\partial \phi / \partial s_\beta$, where s_α, s_β are the lengths along the α and β lines respectively. The curvature tensor effectively measures the lattice change of orientation along the slip lines. In case of local isotropy, proportionality between the dislocation velocity and the applied slide stress results in proportionality between the plastic strain rates and the deviatoric stresses (Prandtl–Reuss relation). The proportionality factor is like a friction factor of the dislocation motion and is assumed to depend on the yield strength. The macroscopic yield strength is the critical stress that results in incipient motion of the dislocation aggregates at a specific point.

In homogeneous materials, the shear strength, k_c, is constant and the lattice curvature is related to the dislocation density according to

$$\partial \phi / \partial s_\alpha = -a_{3\alpha}, \quad \partial \phi / \partial s_\beta = -a_{3\beta}. \tag{B.1}$$

Suppose that the solution of a homogeneous surface gives slip-line directions that relate to a dislocation density, $a_{3\alpha}$, $a_{3\beta}$, according to Eq. (B.1). Returning to the graded surface, its deformation curvature can be given by

$$\frac{\partial \phi}{\partial s_\alpha} = -a_{3\alpha}^* + \frac{1}{2k_c} \frac{\mathrm{d}k_c}{\mathrm{d}z} \frac{\partial r}{\partial s_\alpha}, \quad \frac{\partial \phi}{\partial s_\beta} = -a_{3\beta}^* + \frac{1}{2k_c} \frac{\mathrm{d}k_c}{\mathrm{d}z} \frac{\partial z}{\partial s_\beta}. \tag{B.2}$$

It is clear that if the slip-line solution is the same for both the homogeneous and the graded surfaces, then the corresponding dislocation distributions should be connected as

$$a_{3\alpha}^* = a_{3\alpha} + \frac{1}{2k_c}\frac{dk_c}{dz}\frac{\partial r}{\partial s_\alpha}, \quad a_{3\beta}^* = a_{3\beta} + \frac{1}{2k_c}\frac{dk_c}{dz}\frac{\partial z}{\partial s_\beta}. \tag{B.3}$$

Eqs. (B.1) and (B.3) imply that both the homogeneous and the graded material would have the same deformation curvature, if the dislocation distribution tensor in the graded material has a pre-existing part given by the second terms of the left-hand-side of Eq. (B.3).

References

ABAQUS, 1998. Version 5.7. Finite element code. Hibbitt, Karlsson and Sorensen, Inc., Pawtucket, RI.

Alfredsson, B., Olsson, M., 1999. Standing contact fatigue. Fatigue Fract. Eng. Mater. Struct. 22, 225–237.

Arutiunian, N.Kh., 1959. The plane contact problem in the theory of creep. PMM 23, 1283–1313.

Brenner, P., Kostrov, H., 1950. Macro and micro-segregation in ingots of two aluminium alloys. Metallurgia 41, 209–218.

Burnett, P.J., Page, T.F., 1984. Surface softening in silicon by ion implantation. J. Mater. Sci. 19, 845–860.

Castaneda, P.P., Suquet, P., 1998. Nonlinear composites. Adv. Appl. Mech. 34, 171–301.

Dienes, G.J., Vineyard, G.H., 1957. Radiation Effects in Solids. Interscience Publishers, New York.

Elghazal, H., Lormand, G., Hamel, A., Girodin, D., Vincent, A., 2001. Microplasticity characteristics obtained through nano-indentation measurements: application to surface hardened steels. Mater. Sci. Eng. A 303, 110–119.

Fisher, E.S., Westlake, D.G., Ockers, S.T., 1975. Effects of hydrogen and oxygen on the elastic moduli of vanadium, niobium and tantalum single crystals. Phys. Stat. Sol. A 28, 591–602.

Fourie, J.T., 1968. The flow stress gradient between the surface and centre of deformed copper single crystals. Philos. Mag. Ser. B 17, 735–756.

Fyodorov, A.V., 1990. Fatigue strength improvement by ion implantation. In: Kitagawa, H., Tanaka, T. (Eds.), Proceedings of the Fourth International Conference on Fatigue and Fatigue Thresholds, pp. 293–298.

Giannakopoulos, A.E., Suresh, S., 1997. Indentation of solids with gradients in elastic properties. Part I: Point force, Part II: Axisymmetric indenters. Int. J. Solids Struct. 34, 2357–2428.

Holder, J., Granato, A.V., Rehn, L.E., 1974. Effects of self-interstitials and close pairs on the elastic constants of copper. Phys. Rev. B 10, 363–375.

Hill, R., 1950. The Mathematical Theory of Plasticity. Clarendon Press, Oxford.

Kroner, E., 1958. Kontinuum Theorie Der Versetzungen und Eigenspannungen. Springer, Berlin.

Lawn, B.R., Evans, A.G., Marshall, D.B., 1980. Elastic/plastic indentation damage in ceramics: The median/radial crack system. J. Am. Ceram. Soc. 63, 574–581.

Lockett, F.J., 1963. Indentation of a rigid/plastic material by a conical indentor. J. Mech. Phys. Solids 11, 345–355.

Marshall, D.B., Lawn, B.R., Evans, A.G., 1982. Elastic/plastic indentation damage in ceramics: The lateral crack system. J. Am. Ceram. Soc. 65, 561–566.

Meyer, R.A., 1954. Influence of deuteron bombardment and strain hardening on notch sensitivity of mild steel. J. Appl. Phys. 25, 1369–1374.

Morrison, D.J., Jones, J.W., Was, G.S., 1990. Microstructural stability of ion implanted surfaces and their effects on fatigue damage accumulation. In: Kitagawa, H., Tanaka, T. (Eds.), Proceedings of the Fourth International Conference on Fatigue and Fatigue Thresholds, pp. 287–292.

Mott, B.W., 1956. Micro-indentation Hardness Testing. Butterworths, London.

Mughrabi, H., 1971. Some consequences of surface size effects in plastically deformed copper single crystals. Phys. Stat. Sol. (b) 44, 391–402.

Mura, T., 1965. Continuous distribution of dislocations and the mathematical theory of plasticity. Phys. Stat. Sol. 10, 447–453.

Myers, S.M., Knapp, J.A., Follstaedt, D.M., Dugger, M.T., 1998. Mechanical properties of nickel ion-implanted with titanium and carbon and their relation to microstructure. J. Appl. Phys. 83, 1256–1264.

Nastasi, M., Mayer, J.W., Hirvonen, J.K., 1998. Ion-Solid Interactions: Fundamentals and Applications. Cambridge University Press, Cambridge, UK.

Pethica, J.B., Hutchings, R., Oliver, W.C., 1983. Composition and hardness profiles in ion implanted metals. Nucl. Instrum. Methods 209–210, 995–1000.

Richmond, O., Morrison, H.L., 1968. Application of a perturbation technique based on the method of characteristics to axisymmetric plasticity. J. Appl. Mech. 35, 117–122.

Shield, R.T., 1955. On the plastic flow of metals under conditions of axial symmetry. Proc. R. Soc. London A 233, 267–287.

Simpson, H.M., Kerkhoff, S.J., 1976. The interaction of point defects with dislocations in high purity copper above room temperature: I Electron irradiation. Radiat. Eff. 27, 191–198.

Spencer, A.J.M., 1961. Perturbation methods in plasticity—I plane strain of non- homogeneous plastic solids. J. Mech. Phys. Solids 9, 279–288.

Stephens, L.S., Liu, Y., Meletis, E.I., 2000. Finite element analysis of the initial yielding behavior of a hard coating/substrate system with functionally graded interface under indentation and friction. J. Tribol. 122, 381–387.

Tartaglia, J.M., Eldis, G.T., 1984. Core hardenability calculations for carburizing steels. Metall. Trans. A 15, 1173–1183.

Zinkle, S.J., Oliver, W.C., 1986. Mechanical property measurements on ion-irradiated copper and Cu–Zr. J. Nucl. Mater. 141–143, 548–552.